

# Visualization of quantum interferences in heavy-ion elastic scattering

Kyoungsu Heo

*Department of Physics and Origin of Matter and Evolution of Galaxies (OMEG) Institute, Soongsil University, Seoul 06978, Korea*

K. Hagino

*Department of Physics, Kyoto University, Kyoto 606-8502, Japan*

(Dated: January 17, 2025)

We investigate various interference effects in elastic scattering of the  $\alpha + {}^{40}\text{Ca}$  system at  $E_{\text{lab}} = 29$  MeV. To this end, we use an optical potential model and decompose the scattering amplitude into four components, that is, the near-side and the far-side components, each of which is further decomposed into the barrier-wave and the internal-wave components. Each component contributes distinctively to the angular distributions, revealing unique quantum interference patterns. We apply the Fourier transform technique to visualize these interference effects. By analyzing the images at specific scattering angles, we identify the positions and intensities of peaks corresponding to each interference component. This analysis offers insight into structural features of the angular distribution which are not apparent from the differential cross sections alone.

## I. INTRODUCTION

Differential cross sections,  $d\sigma/d\Omega$ , obtained from nuclear scattering experiments represent a cumulative result of all quantum mechanical interactions between a projectile and a target nuclei. However, this observable alone may not directly reveal the complex quantum interference effects that occur during the scattering process. A differential cross section is the square of a scattering amplitude,  $f(\theta)$ , combining all interference effects into a single measurement. Thus, to gain deeper insight into the physical mechanisms governing the scattering process, it is helpful to analyze the scattering amplitude itself and disentangle the underlying interference patterns, even though the scattering amplitude is not an observable.

For collisions at energies well below the Coulomb barrier, the scattering amplitude is dominated by the Coulomb amplitude,  $f_C(\theta)$ . In collisions of identical spin-0 boson particles, such as  ${}^{16}\text{O} + {}^{16}\text{O}$  and  ${}^{12}\text{C} + {}^{12}\text{C}$ , the scattering amplitude can then be described using the Coulomb scattering amplitude as  $f(\theta) = f_C(\theta) + f_C(\pi - \theta)$  [1, 2] after taking into account the symmetrization of the wave function. See Ref. [3] for scattering of identical nuclei with arbitrary spin. The resultant cross sections become symmetric with respect to  $\theta = \pi/2$  and show characteristic oscillations due to the interferences between  $f_C(\theta)$  and  $f_C(\pi - \theta)$ .

As the incident energy increases above the Coulomb barrier, nuclear interactions become more significant, absorbing a part of the elastic flux, and thereby the angular distributions reveal a more complex pattern [4, 5]. These effects are particularly pronounced in light heavy-ion systems. The  $\alpha + {}^{40}\text{Ca}$  system is of particular interest in this regard, as light projectiles like  $\alpha$ -particles exhibit strong nuclear binding, leading to distinctive nuclear rainbow patterns in elastic scattering [6]. This is a system with a weak absorption, and elastic scattering cross sections tend to increase at large angles, producing

refractive effects akin to optical rainbows. This occurs when a part of the elastic flux is refracted by the nuclear interaction between the  $\alpha$ -particle and the target nucleus. In addition, cross sections often show anomalously large enhancements at backward angles, likely due to a weak absorption [7]. This is referred to as anomalous large-angle scattering (ALAS).

The nuclear rainbow effects can be interpreted as a consequence of interferences between the near-side and the far-side components of scattering amplitudes [8, 9]. Here, near-side scattering is associated with positive scattering angles dominated by a repulsive Coulomb interaction, while far-side scattering corresponds to negative angles influenced by an attractive nuclear potential. The interference between these two components leads to characteristic oscillatory patterns in differential cross sections, particularly at small and intermediate angles. By isolating these interference effects through a nearside-farside decomposition, one can gain a clearer understanding of the underlying physical mechanisms of oscillations in angular distributions[8].

On the other hand, the ALAS can be interpreted as a consequence of interferences between a barrier-wave and an internal-wave [10]. Here, a barrier-wave corresponds to a reflected wave at the outer turning point of a barrier, while an internal-wave corresponds to a wave which penetrates the Coulomb barrier and reflects at the innermost turning point. This was initially proposed by Brink and Takigawa [10] and later refined for computational efficiency in Ref. [11]. This approach is particularly effective when the nuclear potential features a potential pocket, allowing for distinct turning points that facilitate component separation in the scattering process. Interferences between the barrier wave and the internal wave yield complex oscillatory patterns in angular distributions, which are particularly prominent in weakly absorbing systems, such as  $\alpha + {}^{40}\text{Ca}$ . The barrier-wave-internal-wave decomposition is useful in examining scattering processes where a projectile retains transparency,

as is seen in scattering systems involving a composite particle such as an  $\alpha$ -particles.

Recently, it was proposed to take a Fourier transform of scattering amplitudes and visualize scattering process [12]. This method was applied to the nearside-farside interferences in  $^{16}\text{O}+^{16}\text{O}$  elastic scattering [2], providing an intuitive interpretation of interference effects by creating images of scattering centers on a virtual screen. In this way, this approach provides a deeper understanding of how scattering patterns evolve with incident energies and how the interference between different components affects the overall scattering process. That is, this method offers a novel perspective on the complex nuclear interactions at play and is expected to shed light on the fundamental structure of nuclear interactions.

In this paper, we apply the same technique to  $\alpha+^{40}\text{Ca}$  scattering. To this end, we decompose the scattering amplitudes into four components: the nearside-barrier-wave, the nearside-internal-wave, the far-side-barrier-wave, and the far-side-internal-wave components. Such combined decomposition between the nearside-farside and the barrier-wave-internal-wave components was first introduced in Ref. [13] for the  $^{16}\text{O}+^{16}\text{O}$  system. Each component distinctly contributes to the scattering process, resulting in complex interference patterns in the angular distribution. We shall discuss how these four components are visualized by the Fourier transform technique.

The paper is organized as follows. In Sec. II, we analyze the angular distribution of the  $\alpha+^{40}\text{Ca}$  scattering at  $E_{\text{lab}} = 29$  MeV using an optical model. We will decompose the scattering amplitudes into the four components, that is, the nearside-barrier, the nearside-internal, the farside-barrier, and the farside-internal components. In Sec. III, we introduce the imaging technique and analyze the scattering amplitudes by taking the Fourier transform. We will discuss the origin of each peak in the image by taking the Fourier transform of each component of the scattering amplitudes. We will then summarize the paper in Sec. IV.

## II. DECOMPOSITION OF SCATTERING AMPLITUDES

We consider the elastic scattering of the  $\alpha+^{40}\text{Ca}$  system at the incident energy of 29 MeV as an example. To this end, we employ the potential B in Ref. [14] given by,

$$V(r) - iW(r) = Uf^2(r, d_1, b_1) - i \left[ W_v df^2(r, d_2, b_2) - 4b_3 W_D \frac{d}{dr} f^2(r, d_3, b_3) \right] \quad (1)$$

with the function  $f(r, d_i, b_i)$  given by:

$$f(r, d_i, b_i) = \left( 1 + \exp \left( \frac{r - d_i A_T^{1/3}}{b_i} \right) \right)^{-1}, \quad (2)$$

$A_T$  being the mass number of the target nucleus. We use the depth parameters of  $U = 173.14$  MeV,  $W_v = 6.67$  MeV, and  $W_D = 46.92$  MeV, while the geometric parameters of  $d_1 = 1.41$  fm,  $b_1 = 1.24$  fm,  $d_2 = 1.00$  fm,  $d_3 = 0.62$  fm, and  $b_3 = 1.04$  fm.

The differential cross sections for the energy  $E = k^2 \hbar^2 / 2\mu$ ,  $k$  and  $\mu$  being the wave number and the reduced mass, respectively, are given by

$$\frac{d\sigma}{d\Omega} = |f(\theta)|^2, \quad (3)$$

where the scattering amplitude  $f(\theta)$  for a scattering angle  $\theta$  is computed as

$$f(\theta) = f_C(\theta) + \sum_{l=0}^{\infty} (2l+1) \frac{S_l - 1}{2ik} P_l(\cos \theta). \quad (4)$$

Here,  $f_C(\theta)$  is the Coulomb scattering amplitude,  $S_l$  is the nuclear  $S$ -matrix for the  $l$ -th partial wave, and  $P_l(\cos \theta)$  is the Legendre polynomial. The angular distribution obtained with this potential is shown by the solid line in Fig. 1, which well reproduces the experimental data.

To clarify the oscillating patterns in the angular distribution, let us first decompose the scattering amplitudes into the nearside component  $f_N(\theta)$  and the farside component  $f_F(\theta)$ , that is,  $f(\theta) = f_N(\theta) + f_F(\theta)$ . To separate the nearside and the farside contributions, we follow Ref. [9] and replace the Legendre polynomials  $P_l(\cos \theta)$  in Eq. (4) with complex combinations that selectively isolate these trajectories:

$$P_l(\cos \theta) \rightarrow \tilde{Q}_l^{(\pm)}(\cos \theta) = \frac{1}{2} \left[ P_l(\cos \theta) \pm \frac{2i}{\pi} Q_l(\cos \theta) \right], \quad (5)$$

where  $Q_l(\cos \theta)$  is the Legendre function of the second kind. Here,  $\tilde{Q}_l^{(-)}(\cos \theta)$  corresponds to the nearside scattering with positive deflection angles, while  $\tilde{Q}_l^{(+)}(\cos \theta)$  corresponds to the farside scattering with negative deflection angles. This replacement defines the nearside and the farside amplitudes as follows:

$$f_N(\theta) = \sum_{l=0}^{\infty} (2l+1) \frac{S_l - 1}{2ik} \tilde{Q}_l^{(-)}(\cos \theta) + f_N^{(C)}(\theta), \quad (6)$$

$$f_F(\theta) = \sum_{l=0}^{\infty} (2l+1) \frac{S_l - 1}{2ik} \tilde{Q}_l^{(+)}(\cos \theta) + f_F^{(C)}(\theta), \quad (7)$$

where  $f_N^{(C)}(\theta)$  and  $f_F^{(C)}(\theta)$  are the nearside and the farside components of the Coulomb amplitude,  $f_C(\theta)$  [9].

The scattering amplitudes can be decomposed in another way, that is, into to the barrier wave scattering amplitude,  $f_B(\theta)$ , representing reflections at the Coulomb barrier, and the internal wave scattering amplitude  $f_I(\theta)$ , associated with reflections within the nuclear potential pocket. Those two scattering amplitudes are given as

$$f(\theta) = f_B(\theta) + f_I(\theta) \quad (8)$$

with

$$f_B(\theta) = \sum_{l=0}^{\infty} (2l+1) e^{2i\sigma_l} P_l(\cos\theta) [S_B(l) - 1] + f_C(\theta), \quad (9)$$

and

$$f_I(\theta) = \sum_{l=0}^{\infty} (2l+1) e^{2i\sigma_l} P_l(\cos\theta) S_I(l), \quad (10)$$

respectively. In these equations,  $\sigma_l$  is the Coulomb phase shift, while  $S_B(l)$  and  $S_I(l)$  are nuclear phase shifts for the barrier wave and the internal wave, respectively. Following Ref. [11], these are obtained as

$$S_B = \frac{S_+ S_- S_0^2}{S_+ + S_- S_0}, \quad S_I = S_0 - S_B, \quad (11)$$

where  $S_0$  is the phase shift for the original optical potential,  $V(r)$ , while  $S_{\pm}$  are the phase shifts for modified optical potentials,  $V_{\pm}(r) = V(r) \pm \delta V(r)$ . We follow Ref. [11] and take  $\delta V(r) = \pm i W_1 e^{-(r/\rho)^4}$  with  $W_1 = 1.0$  MeV and  $\rho = 3.25$  fm.

By introducing  $\tilde{Q}_l^{(\pm)}$  in Eq. (5) into Eqs. (9) and (10), each of the barrier and the internal wave components can further be decomposed into the near-side and the far-side terms[13]. That is,

$$f(\theta) = \sum_{X=B,I} \sum_{Y=N,F} f_{XY}(\theta), \quad (12)$$

where  $X \in \{B, I\}$  for the barrier and the internal waves and  $Y \in \{N, F\}$  for the nearside and the farside components. This comprehensive decomposition highlights the role of nuclear transparency and absorption in shaping the observed scattering patterns. It provides a robust framework for understanding interference effects, particularly in systems like  $\alpha + {}^{40}\text{Ca}$  at 29 MeV, where both the barrier and the internal wave components play a significant role.

The decomposition of the angular distributions is shown in Fig. 1. The red dashed and the red dotted lines denote the angular distributions for the barrier-farside wave and the barrier-nearside wave components, respectively, while the blue dot-dashed and the blue dot-dot-dashed lines show those for the internal-farside wave and the internal-nearside wave components, respectively. One can notice that the nearside-barrier-wave component dominates at forward angles, particularly below  $40^\circ$ , where the Coulomb interaction plays a significant role. On the other hand, the two internal wave components account for the oscillations observed at larger scattering angles.

### III. VISUALIZATION OF REACTION PROCESSES

To visualize the scattering contributions and the interference effects, let us apply a Fourier transform to

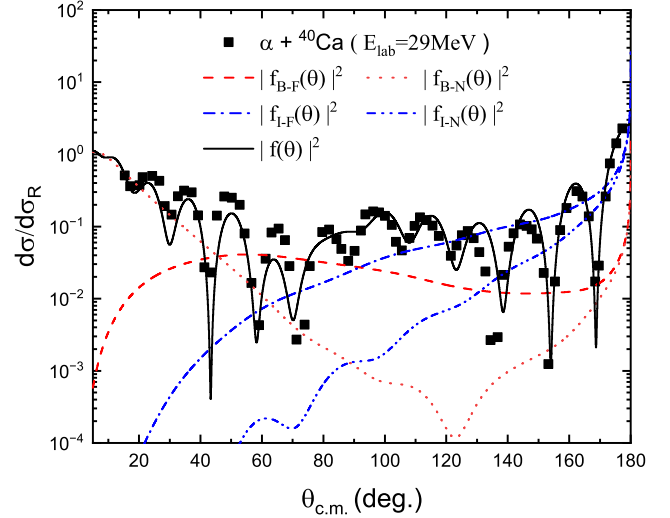


FIG. 1. The angular distribution of elastic scattering for the  $\alpha + {}^{40}\text{Ca}$  system at  $E_{\text{lab}} = 29$  MeV. The black squares represent the experimental data taken from Ref. [14]. The black solid line shows the angular distribution obtained with the optical model calculation. The red dashed, the red dotted, the blue dot-dashed, and the blue dot-dot-dashed lines denote the angular distributions for the barrier-far wave, the barrier-near wave, the internal-far wave, and the internal-near wave components, respectively.

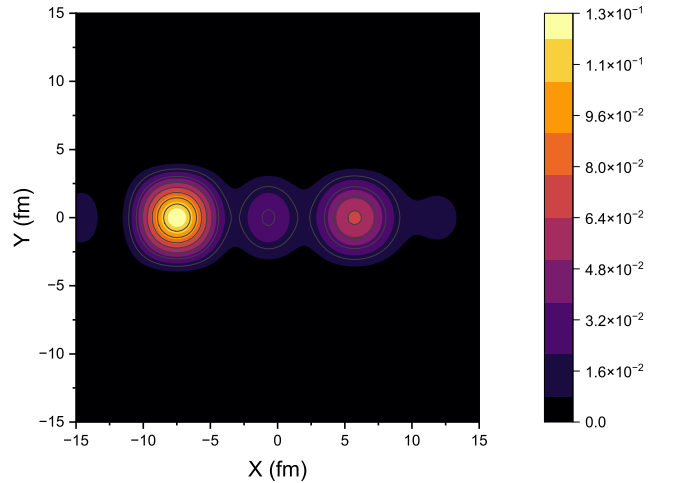


FIG. 2. The image of elastic scattering for  $\alpha + {}^{40}\text{Ca}$  at  $E_{\text{lab}} = 29$  MeV and  $\theta = 64^\circ$ , generated by Fourier transforming the total scattering amplitude. The angular widths are set to be  $\Delta\theta = \Delta\phi = 15^\circ$ .

the scattering amplitudes[2, 12], inspired by techniques from wave optics [15]. This approach transforms angular scattering information of the scattering processes into a spatial image, enabling one to distinguish the interference effects from different scattering paths, such as the nearside-farside and the barrier-wave-internal-wave components. In the imaging process, one introduces a lens to

condense waves on a virtual screen behind the lens. This is formulated as follows:

$$\begin{aligned} \Phi(X, Y) &= \frac{1}{S} \int_{\theta_0 - \Delta\theta}^{\theta_0 + \Delta\theta} d\theta e^{ik(\theta - \theta_0)X} f(\theta) \\ &\times \int_{\phi_0 - \Delta\phi}^{\phi_0 + \Delta\phi} d\phi e^{ik(\phi - \phi_0)Y}, \end{aligned} \quad (13)$$

where  $(X, Y)$  are coordinates on the virtual screen positioned behind the lens located at  $(\theta_0, \phi_0)$  and  $S = 4(\Delta\theta)(\Delta\phi)$  represents the angular area of the lens. Here,  $\theta$  and  $\phi$  denote the scattering angles centered at  $\theta_0$  and  $\phi_0$  with widths  $\Delta\theta$  and  $\Delta\phi$ , respectively. The resulting image intensity, which visually represents the differential cross-section, is given by,

$$I(X, Y) = |\Phi(X, Y)|^2. \quad (14)$$

In cases where the scattering amplitude is independent of  $\phi$ , the integral in the  $Y$ -direction is simplified as [12],

$$\int_{\phi_0 - \Delta\phi}^{\phi_0 + \Delta\phi} d\phi e^{ik(\phi - \phi_0)Y} = 2\Delta\phi \frac{\sin(kY\Delta\phi)}{kY\Delta\phi}, \quad (15)$$

which peaks at  $Y = 0$  with an approximate width of  $2\pi/(k\Delta\phi)$ , defining the resolution in the  $Y$ -direction.

Figure 2 shows the image for the total scattering amplitude. We choose  $\theta_0 = 64^\circ$  as one can observe three distinct peaks in the image at this angle. The angular widths are set to be  $\Delta\theta = \Delta\phi = 15^\circ$ . One can observe the three primary peaks, two on the negative  $X$  side and one on the positive  $X$  side, each with distinct maximum intensities. The peaks observed on the  $-X$  side correspond to negative impact parameters, indicating an attractive potential due to the nuclear interaction and thus the farside component [2]. On the other hand, the peak on the positive  $X$  side corresponds to a positive impact parameter, thus the nearside component [2].

In order to clarify the origin of each peak, particularly the two peaks at negative  $X$ , we decompose the scattering amplitude into the four components as in Eq. (12), and take the Fourier transform for each of the scattering amplitudes. The top, the middle, and the bottom panels in Fig. 3 show the images for the barrier-wave-farside, the internal-wave-farside, and the barrier-wave-nearside, respectively. The internal-wave-nearside component has a relatively low intensity, as is indicated in Fig. 1, and does not appear prominently in the image at this angle, even though it becomes more visible at backward angles. One can now see that the leftmost peak in the image shown in Fig. 2 originates from the barrier-wave-farside component, and the middle peak from the internal-wave-farside component, and the peak at  $+X$  from the barrier-wave-nearside component. This analysis demonstrates that the imaging technique effectively captures and illustrates each interference effect in the scattering process.

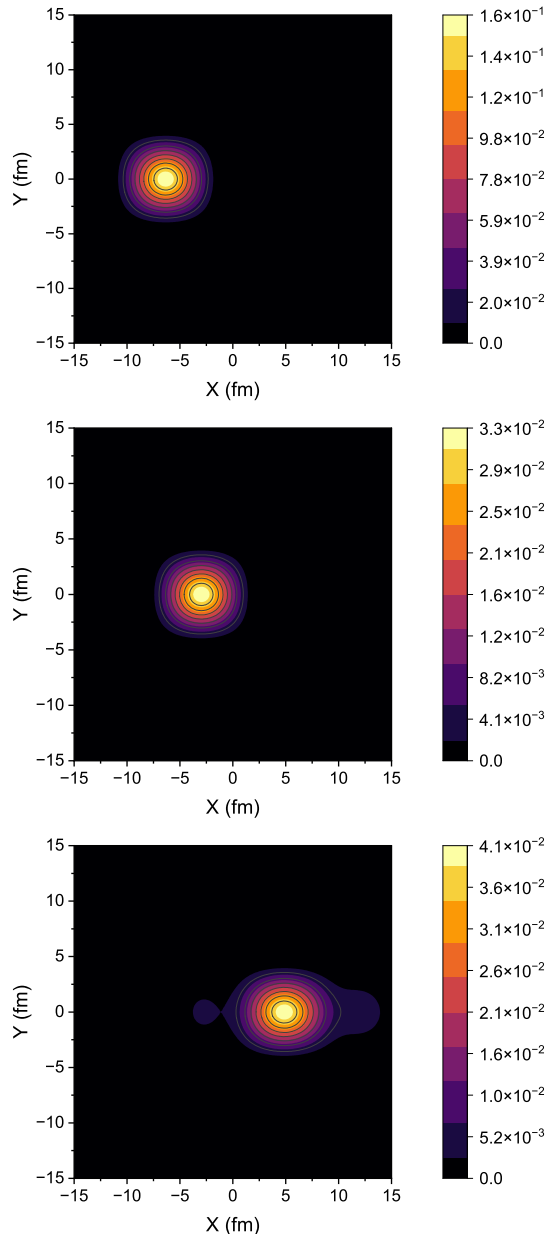


FIG. 3. Same as Fig. 2, but for the images of each component of the scattering amplitude. The top, the middle, and the bottom panels show the images for the barrier-wave-farside, the internal-wave-farside, and the barrier-wave-nearside, respectively.

Fig. 4 shows the imaging results at four different scattering angles,  $\theta = 30^\circ, 64^\circ, 90^\circ,$  and  $150^\circ$ , all computed with  $\Delta\theta = 15^\circ$  and for  $Y = 0$ . At  $\theta = 30^\circ$ , a single prominent peak appears at  $+X$ , corresponding to the barrier-near component. This is consistent with the fact that forward angles are dominated by the barrier wave, and near-side contributions are significant due to the relatively low deflection angles. At  $\theta = 64^\circ$ , which was also analyzed in Figs. 2 and 3, multiple peaks emerge. The main peak at  $-X$  is dominated by the barrier-far com-

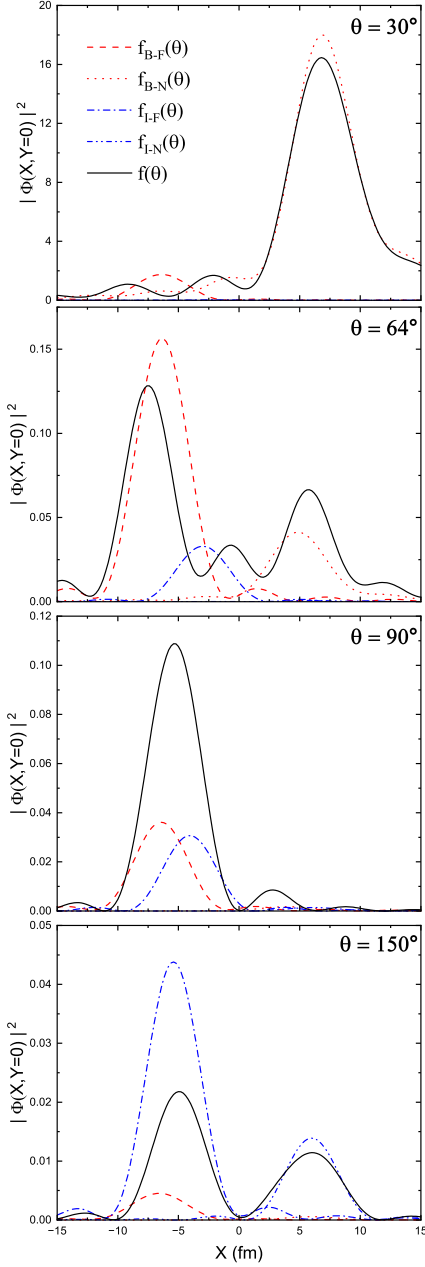


FIG. 4. Imaging results for  $Y = 0$  at four different scattering angles,  $\theta = 30^\circ$ ,  $64^\circ$ ,  $90^\circ$ , and  $150^\circ$ , with  $\Delta\theta = 15^\circ$ . The solid line represents the images from the total scattering amplitude, while the red dashed, the red dotted, the blue dot-dashed, and the blue dot-dot-dashed lines denote the results for the farside-barrier wave, the nearside-barrier-wave, the farside-internal wave, and the nearside-internal wave components, respectively.

ponent, while the central peak around  $X \sim 0$  is due to both the internal-far and the barrier-near components. The peak at  $+X$  is associated with the barrier-near component. This detailed decomposition is consistent with the earlier results and confirms the roles of individual scattering amplitude components at this angle. Notice,

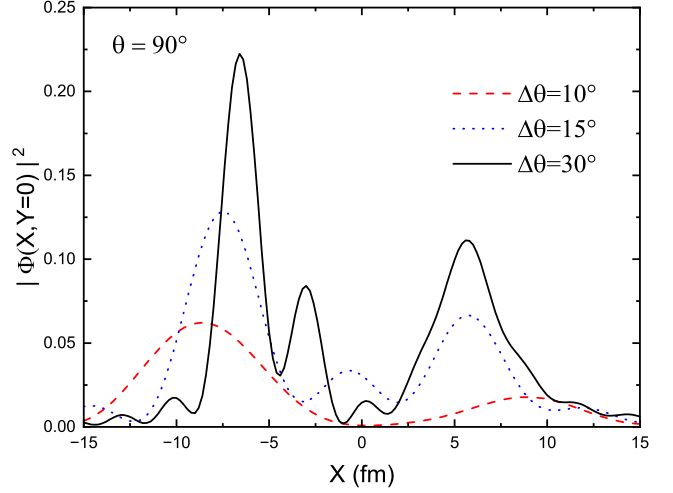


FIG. 5. The image obtained with the total scattering amplitude at  $\theta = 64^\circ$  with three different values of  $\Delta\theta$ .

however, that, due to the interference effects, the peak of each contribution does not necessarily coincide with the peaks for the total amplitude shown by the black solid line. At  $\theta = 90^\circ$ , the imaging result shows a single prominent peak at  $-X$ , which arises from the barrier-far and internal-far components. The near-side contributions are suppressed at this intermediate angle, highlighting the dominance of farside effects. Finally, at  $\theta = 150^\circ$ , two peaks are observed: one at  $-X$  and the other at  $+X$ . The peak at  $-X$  corresponds to the internal-far component, which becomes increasingly significant at backward angles due to the dominance of the internal wave. The peak at  $+X$ , on the other hand, is associated with the internal-near component. This result highlights the growing contribution of the internal wave at large scattering angles, which is consistent with the increased cross sections observed at backward angles.

Overall, the imaging results clearly demonstrate how the contributions of each component of the scattering amplitudes evolve with the scattering angles. By representing the scattering amplitude in terms of  $X$ , which is closely related to the impact parameter [2], the distinction between the far-side and the near-side components becomes immediately apparent. This approach reinforces the utility of imaging techniques for disentangling complex interference patterns in nuclear scattering. Notice that the imaging technique does not require explicit decompositions of the total scattering amplitude to see how many components are contributing to the scattering at a given scattering angle.

We notice that the choice of  $\Delta\theta$  significantly affects the resolution and interpretability of imaging results, as is indicated in Eq. (15). Fig. 5 shows the imaging results for  $\theta = 64^\circ$  and  $Y = 0$  with  $\Delta\theta = 10^\circ$ ,  $15^\circ$ , and  $30^\circ$ . These results, obtained with the total scattering amplitude, demonstrate the trade-offs involved in selecting  $\Delta\theta$ . For  $\Delta\theta = 10^\circ$  (the red dashed line), two primary



peaks are observed. Fine structure of the image, such as the peak around  $X \sim 0$ , are suppressed due to the broad averaging effect of a small  $\Delta\theta$ . For  $\Delta\theta = 15^\circ$  (the blue dotted line), additional structure emerges, revealing three distinct peaks. This result corresponds to the image shown in Fig. 4, confirming the consistent appearance of interference effects. For  $\Delta\theta = 30^\circ$  (the black solid line), more peaks are resolved as individual contributions from overlapping components become separated, leading to finer interference patterns. This comparison highlights the balance between resolution and clarity. Smaller values of  $\Delta\theta$  emphasize the dominant contributions but may obscure the detailed structure of overlapping components. Conversely, larger values of  $\Delta\theta$  provide higher resolution but may sometimes complicate interpretation by revealing numerous peaks. At  $\theta = 64^\circ$ , for instance,  $\Delta\theta = 15^\circ$  provides a practical balance. This value allows for resolving the primary peaks and observing the contributions from different components of the scattering amplitude. At the same time, minor peaks are invisible with this choice of  $\Delta\theta$ , which in this sense is more convenient than  $\Delta\theta = 30^\circ$ .

#### IV. CONCLUSION

We have investigated elastic scattering of the  $\alpha + {}^{40}\text{Ca}$  system at  $E_{\text{lab}} = 29$  MeV using an optical model. We have decomposed the scattering amplitude into the barrier-wave-nearside, the barrier-wave-farside, the internal-wave-nearside, and the internal-wave-farside components, and applied the Fourier transformation techniques to visualize them. In this way, we have iden-

tified the origins of prominent peaks in the image and matched them with the corresponding amplitude components. That is, the image has three prominent peaks at  $\theta = 64^\circ$ , two peaks corresponding to negative impact parameters and one peak corresponding to a positive impact parameter. While the negative impact parameters correspond to the farside components, we have identified that the barrier-wave-farside corresponds to a larger negative impact parameter, compared to the internal-wave-farside component. The peak for a positive impact parameter corresponds to the barrier-wave-nearside component.

The analysis shown in this paper confirms that the imaging technique provides a powerful tool to analyze complex interference patterns in nuclear scattering in an intuitive manner. This method advances our understanding of nuclear reaction dynamics, emphasizing the role of quantum coherence and nuclear transparency in shaping observed scattering phenomena. Our results presented in this paper thus show a novel perspective for interpreting scattering mechanisms in light heavy-ion collisions. It would be an interesting future work to apply this approach to other nuclear reactions, such as proton elastic scattering, for which quantum effects are more prominent than in heavy-ion systems.

#### ACKNOWLEDGMENTS

This research was supported in part by Basic Science Research Program through the National Research Foundation of Korea(NRF) funded by the Ministry of Education(Grant Nos. NRF-2020R1A2C3006177 and RS-2024-00460031) and in part by JSPS KAKENHI Grant Number JP23K03414.

- 
- [1] D. A. Bromley, J. A. Kuehner, and E. Almqvist, *Phys. Rev.* **123**, 878 (1961).
  - [2] K. Hagino and T. Yoda, *Phys. Lett. B* **848**, 138326 (2024).
  - [3] A. J. Toubiana, L. F. Canto, R. Donangelo, and M. S. Hussein, *Phys. Rev. C* **96**, 064615 (2017).
  - [4] R. G. Stokstad, R. M. Wieland, G. R. Satchler, C. B. Fulmer, D. C. Hensley, S. Raman, L. D. Rickertsen, A. H. Snell, and P. H. Stelson, *Phys. Rev. C* **20**, 655 (1979).
  - [5] Y. Sugiyama, Y. Tomita, H. Ikezoe, Y. Yamanouchi, K. Ideno, S. Hamada, T. Sugimitsu, M. Hijiya, and Y. Kondō, *Phys. Lett. B* **312**, 35 (1993).
  - [6] D. T. Khoa, W. von Oertzen, H. G. Bohlen, and S. Ohkubo, *J. of Phys. G* **34**, R111 (2007).
  - [7] R. Planeta, H. Dabrowski, L. Freindl, and K. Grotowski, *Nucl. Phys. A* **326**, 97 (1979).
  - [8] M. Hussein and K. McVoy, *Prog. in Part. Nucl. Phys.* **12**, 103 (1984).
  - [9] R. C. Fuller, *Phys. Rev. C* **12**, 1561 (1975).
  - [10] D. M. Brink and N. Takigawa, *Nucl. Phys. A* **279**, 159 (1977).
  - [11] J. Albiński and F. Michel, *Phys. Rev. C* **25**, 213 (1982).
  - [12] K. Hashimoto, Y. Matsuo, and T. Yoda, *Prog. Theor. Exp. Phys.* **2023**, 043B04 (2023).
  - [13] F. Michel, G. Reidemeister, and S. Ohkubo, *Phys. Rev. C* **63**, 034620 (2001).
  - [14] T. Delbar, G. Grégoire, G. Paic, R. Ceuleneer, F. Michel, R. Vanderpoorten, A. Budzanowski, H. Dabrowski, L. Freindl, K. Grotowski, S. Micek, R. Planeta, A. Strzalkowski, and K. A. Eberhard, *Phys. Rev. C* **18**, 1237 (1978).
  - [15] K. Hashimoto, S. Kinoshita, and K. Murata, *Phys. Rev. Lett.* **123**, 031602 (2019).